Corrected 11 March 2016; see full text.

CELL NUCLEUS

Visualizing the molecular sociology at the HeLa cell nuclear periphery

Julia Mahamid,[1]* Stefan Pfeffer,[1] Miroslava Schaffer,[1] Elizabeth Villa,[1,2] Radostin Danev,[1] Luis Kuhn Cuellar,[1] Friedrich Förster,[1] Anthony A. Hyman,[3] Jürgen M. Plitzko,[1] Wolfgang Baumeister[1]*

The molecular organization of eukaryotic nuclear volumes remains largely unexplored. Here we combined recent developments in cryo–electron tomography (cryo-ET) to produce three-dimensional snapshots of the HeLa cell nuclear periphery. Subtomogram averaging and classification of ribosomes revealed the native structure and organization of the cytoplasmic translation machinery. Analysis of a large dynamic structure—the nuclear pore complex—revealed variations detectable at the level of individual complexes. Cryo-ET was used to visualize previously elusive structures, such as nucleosome chains and the filaments of the nuclear lamina, in situ. Elucidation of the lamina structure provides insight into its contribution to metazoan nuclear stiffness.

Cellular functions arise from an intricate network of macromolecular interactions. Hence it is of fundamental importance to decipher this "molecular sociology" of cells, ideally by direct visualization (*1*). Cryo–electron tomography (cryo-ET) provides three-dimensional (3D) images of cellular landscapes at increasingly higher resolutions; with cellular fractionations, subnanometer resolutions have been attained (*2*, *3*). Structural investigations in situ sensu stricto are more challenging owing to a number of limitations, which can now be overcome; (i) cryo–focused ion beam (FIB) micromachining has opened windows into frozen-hydrated cells and tissues, otherwise too thick to be examined directly by transmission electron microscopy (TEM) (*4*–*7*). However, freestanding lamellas produced by cryo-FIB have little contact with the conductive support film, increasing the likelihood of beam-induced specimen charging in the TEM (*8*, *9*). We resolved this by sputtering a fine metal coating onto the FIB-lamellas, as routinely applied for biological cryo–scanning electron microscopy (SEM) imaging (*10*). (ii) Direct detectors improve the quality of cryo-TEM images substantially (*11*), and (iii) the recently developed Volta phase plate (VPP) enhances (phase) contrast especially for lower spatial frequencies without the need of defocusing, rendering the tomograms directly interpretable (*9*, *12*, *13*). Here, we combined these developments to produce in situ high-resolution 3D snapshots of the HeLa cell nuclear periphery.

HeLa cells expressing β-tubulin:green fluorescent protein and histone2B:mCherry were cultured on TEM grids, vitrified by plunge freezing, and subsequently observed by cryo–fluorescence microscopy (*14*). Interphase cells were thinned by FIB milling (fig. S1, A and B). A central slice through a cell is generated by removing the biological material above and below an area of interest, resulting in a 200-nm-thick lamella traversing the whole cell (figs. S1, C and D, and S2). Data acquired with the VPP on nonconductive (uncoated) lamellas resulted in distorted images (fig. S3). The

[1]Max Planck Institute of Biochemistry, Department of Molecular Structural Biology, Am Klopferspitz 18, 82152 Martinsried, Germany. [2]Department of Chemistry and Biochemistry, University of California, San Diego, CA, USA. [3]Max Planck Institute of Molecular Cell Biology and Genetics, Pfotenhauerstrasse 108, 01307 Dresden, Germany
*Corresponding author. E-mail: mahamid@biochem.mpg.de (J.M.); baumeist@biochem.mpg.de (W.B.)

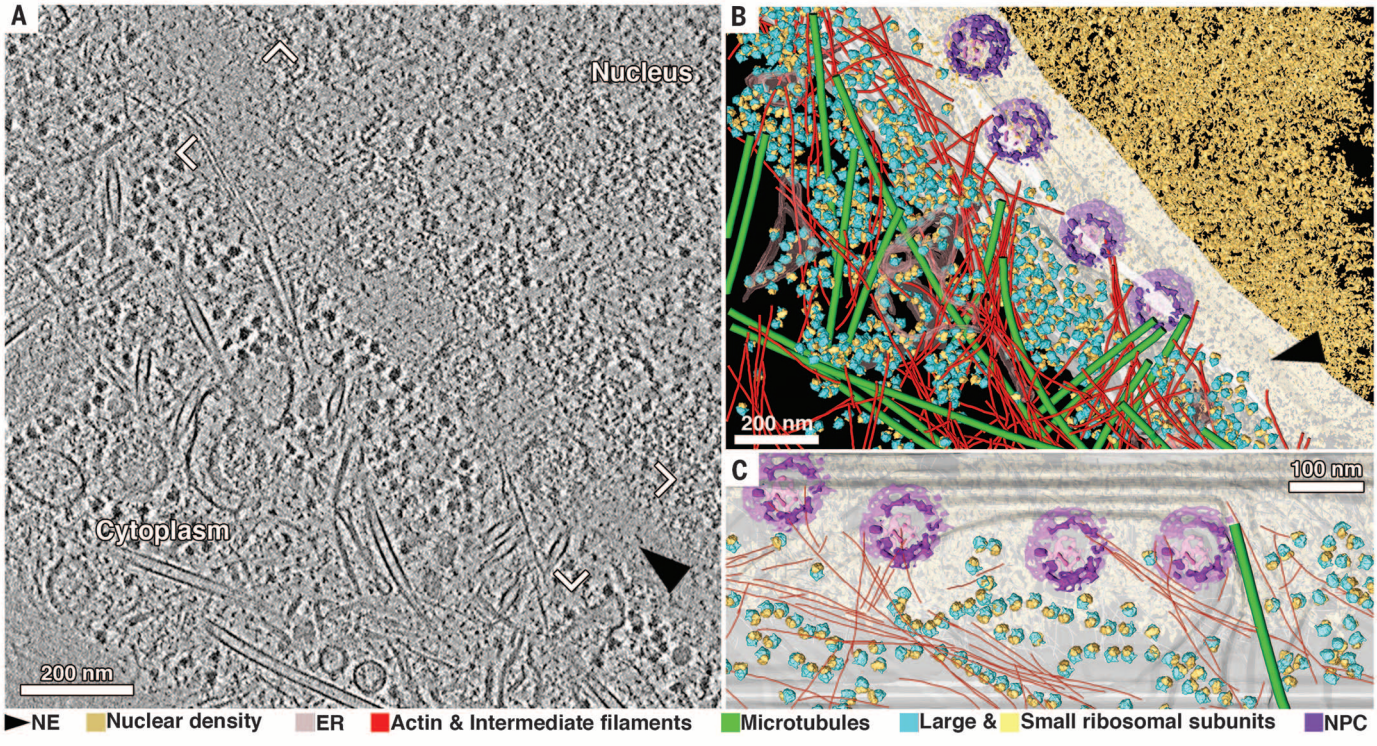

Fig. 1. The nuclear periphery of a HeLa cell revealed by cryo-ET. (**A**) Tomographic slice with 8.4-nm thickness of an interphase HeLa cell thinned by cryo-FIB. (**B**) Annotated view of the tomographic data. Color labels are defined for each structure in (B) and (C). (**C**) Cross-section view of the segmentation in the vicinity of the nuclear envelope [frame in (A)]. NE: nuclear envelope; ER: endoplasmic reticulum; NPC: nuclear pore complex.

Corrected 11 March 2016; see full text.

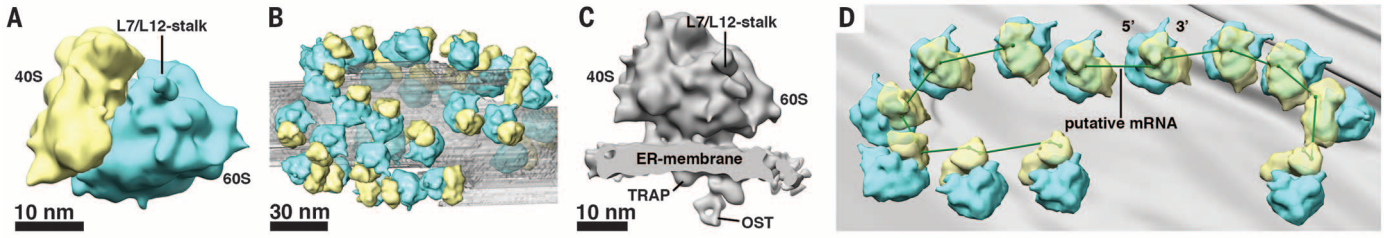

Fig. 2. Subvolume averages of ribosomes and 3D analysis of polysomes. (**A**) Average of cytoplasmic ribosomes. (**B**) ER-associated ribosomes were selected on the basis of their proximity to segmented ER-membranes and averaged independently in (**C**)**:** Side view shows ER-luminal densities of the translocation machinery; TRAP: translocon-associated protein complex; OST: oligosaccharyltransferase. (**D**) Representative polysomes on the NE membrane traced by an automatic approach.

Fig. 3. The molecular organization at the nuclear envelope. Consecutive tomographic slices (8.4 nm) along the nucleocytoplasmic axis. Dashed lines indicate the center positions of three NPCs. (**A**) Density inside the nucleus. Inset: chains of nucleosomes (arrowheads). (**B**) Nuclear lamina. Inset: segmentation of putative lamina filaments. (**C**) NPCs within the NE. Inset: magnified central NPC. Arrowhead: ring density in the luminal space with radial connections to the protomer density. (**D**) The outer NE. Inset: magnified central NPC. (**E**) Polysomes and cytoskeletal filaments at the NE. IF: intermediate filaments. MT: microtubules.

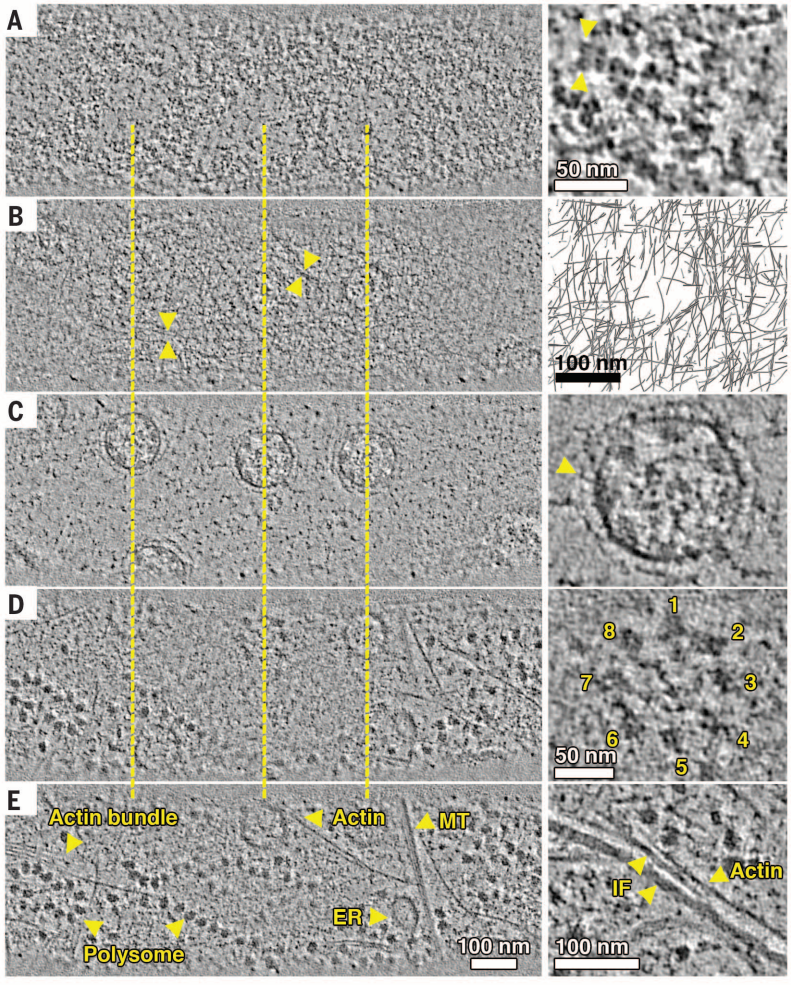

charges building up on the sample produced a field similar to that of an electrostatic lens and led to detrimental beam deformations at the phase plate plane. Thus, a thin platinum layer (<5 nm) was sputtered after lamella preparation to improve conductivity (fig. S2). Our reconstructed volumes acquired with the VPP exhibit high contrast, which allowed for direct visualization and identification of molecular complexes inhabiting the nucleus and the nuclear envelope (NE) (Fig. 1 and movie S1).

To provide a quantitative measure for the attained resolution, we subjected 80*S* ribosomes to subvolume averaging. Cytoplasmic ribosomes from a single tomogram (900 particles) yielded an average with a resolution of 28 Å (Fig. 2A and fig. S4A). Subsequently, ribosomes were sorted according to their spatial association to either the endoplasmic reticulum (ER) or the NE outer membrane (Fig. 2, B and D). An average of the ER-bound fraction (143 particles) yielded a resolution of 35 Å (Fig. 2C and fig. S4A). ER-luminal densities of the translocon-associated protein (TRAP) complex and the oligosaccharyltransferase (OST) complex (*15*) were clearly rendered in ER- and NE-bound particles (Fig. 2C and fig. S4, B to D). Further classification revealed that OST is found on 33% of ER-translocon complexes, in agreement with the stoichiometry of OST observed with isolated rough-ER vesicles (*15*).

Subtomogram averaging of individual ribosomes yielded additional densities in close proximity, indicating arrangement into polysomes with a topology dictated by membrane association (fig. S4E) (*16*). Clustering of the angles describing relative neighbor positions and orientations (fig. S5A) revealed two highly populated classes

Corrected 11 March 2016; see full text.

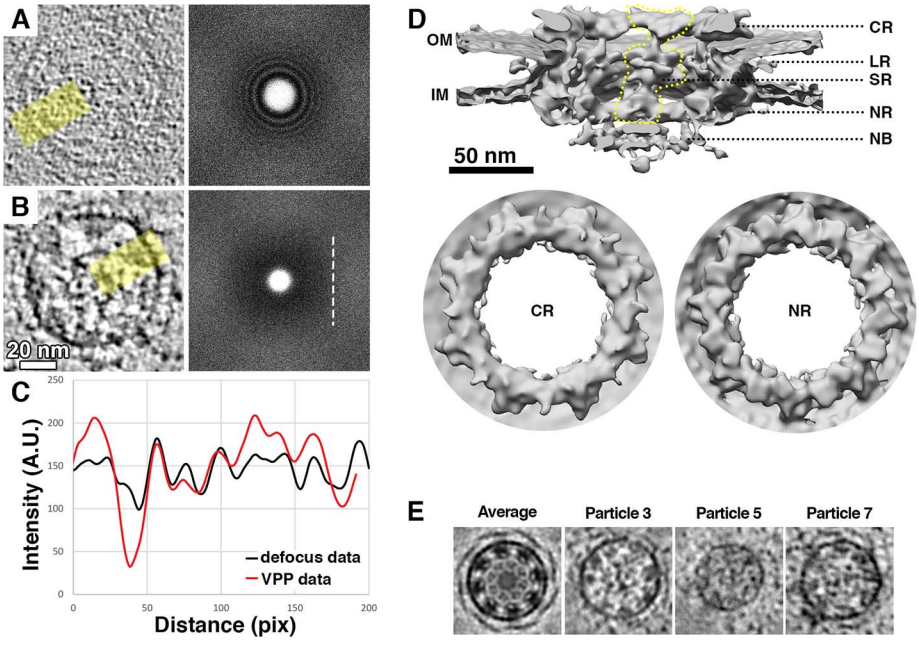

Fig. 4. Tomographic reconstruction and average of the nuclear pore complex. (**A**) Tomographic slices (8.4 nm) obtained at 6-μm defocus (right: FFT at zero tilt) and (**B**) with VPP at 700-nm defocus (right: FFT at zero tilt; dashed line indicates first zero). (**C**) Intensity profiles within yellow boxes in (A) and (B). (**D**) Average of NPCs perpendicular to (top: a protomer is delineated by dashed yellow line) and along the nucleo-cytoplasmic axis (bottom, higher threshold). CR: cytoplasmic ring; OM: outer membrane; LR: luminal ring. SR: spoke ring; IM: inner membrane; NR: nuclear ring. NB: nuclear basket. (**E**) Filtered 2D central slices of the average and representative particles.

representing the left and right neighbors within the same polysome (fig. S5B), in which mRNA entry and exit sites of adjacent ribosomes allow threading of an interconnecting mRNA molecule on a smooth path (fig. S5C). We then performed automatic tracing of polysomes to quantify ribosome organization at the level of individual polysomes (Fig. 2D and table S1) (*14*). A large fraction of membrane-bound ribosomes were associated into polysomes comprising up to 10 particles and exhibiting a close-packed arrangement with a mean distance of 28 nm. This analysis provided a detailed description of the native structure and organization of the cytoplasmic translation machinery in human cells, recapitulating information obtained from microsomes (*15*, *16*) in a single in situ data set.

Large complexes tend not to be strictly deterministic and are often subject to functional and structural variations, which are obscured by averaging. We therefore set to investigate whether the quality of our data would allow characterization of individual complexes. A cross-sectional view of the NE (Figs. 1C and 3) shows four nuclear pore complexes (NPCs), in which we visually identified the eight protomers at the level of the spoke (Fig. 3C) and the cytoplasmic rings (Fig. 3D). An additional ring density surrounding the membrane is distinguished within the NE lumen at the level of the spoke ring (Fig. 3C, inset: arrowhead). Structures at these positions were previously described as discrete luminal densities (*17*, *18*). Here, these densities formed a complete flexible ring with radial connections to the protomers.

The superior contrast provided by the VPP is demonstrated in comparison to data acquired at 6-μm defocus (fig. S6). Density profiles of the NPC obtained from data acquired with and without the VPP show similar variation in the intensities (Fig. 4, A to C). However, the contrast is improved by almost 60% with the VPP despite a lower electron dose (60 e/Å^2 with VPP versus 100 e/Å^2 with defocus). This allowed us to examine previously reported variations in NPC diameter (*17*, *18*). We extracted subvolumes of eight complete NPCs from three interphase cells and performed alignment and averaging. The average reproduced the densities for the cytoplasmic and nuclear rings previously described for the human NPC obtained both in situ and from purified nuclei (Fig. 4D and fig. S7) (*18*, *19*). Deviations from previous structures were evident for the pore diameter in the spoke ring (fig. S7C). We determined the membrane circumference at the spoke ring level for each of the eight particles and our average and found up to 13% difference in the mean particle diameter between the individual pores (Fig. 4E, fig. S8, and table S2). Within the same particle, we observed radial variations of up to 18%. Complexes from the same cells were more homogeneous among themselves, a phenomenon recapitulated in the averages (fig. S8 and table S2), pointing to the intriguing possibility that variations in pore dimensions are related to specific physiological states. This confirmed previous observations of NPC plasticity and illustrates the problem of analyzing large flexible structures by averaging methods. At the same time, it emphasizes the importance of obtaining high-quality primary data allowing analysis of individual complexes.

A network of intermediate filaments, forming the nuclear lamina underlying the NE, is thought to provide mechanical support to the nucleus (*20*). TEM images of the lamina are rare (*21*, *22*), and 10-nm-diameter filaments arranged on an orthogonal lattice have been described in preparations of Triton-extracted and metal-shadowed oocyte NEs (*20*). Here, a volume of 30 nm in thickness underlying the NE is dominated by entangled, 4-nm-diameter filaments (Fig. 3B and fig. S9, B and C). The filaments' diameter in the somatic HeLa cells is in agreement with molecular models proposed for the structure of lamins; namely, dimers of coiled-coils assembled head-to-tail (*23*).

Segmentation of such thin structures is challenging; nevertheless, careful inspection of traced filaments allowed us to obtain an estimate of their flexibility. We measured a persistence length of ~560 nm (fig. S10 and table S3), well within the range described for intermediate filaments and lamins obtained ex situ (*22*–*25*). However, the small filament diameter determined herein resulted in a radically higher elastic modulus for the putative lamina fibrils than what could previously be derived based on a diameter of 10 nm (*14*). An elastic modulus of 190 MPa calculated for the individual filaments recapitulates measurements on whole nuclei, primarily attributed to lamin A (*26*), suggesting that the fine isotropic matrix is the key player in conferring high stiffness to metazoan nuclei.

The complex molecular organization at the NE is demonstrated in Fig. 3. Nuclear volumes exhibit regions of dense material, wherein chains of 10-nm-diameter toroid densities are observed (Fig. 3A and fig. S9A). The morphology of the abundant nuclear complexes is reminiscent of nucleosome core particles (*27*) arranged in a staggered conformation of nucleosome chains (*28*). The clarity with which the individual complexes are discerned should allow unambiguous localization of single nucleosomes by template matching (*29*) and determining their connectivity. Variations in chromatin density correlate with the appearance of the lamina filaments, and they are both diminished in the vicinity of NPCs (Fig. 3, A and B). Extensive polysomes reside on the outer

Corrected 11 March 2016; see full text.

NE membrane (Fig. 3, D and E). The cytoplasm contains filaments of the cell's cytoskeleton, distinguishable according to size and morphology: actin fibers with a helical pitch, smooth intermediate filaments of variable diameters, and 13-protofilament microtubules (Fig. 3E and fig. S10). Occasionally, actin filaments formed direct physical connections to NPCs (Fig. 3E). With the NPCs embedded within the stiff lamina on one side and directly connected to the cytoskeleton on the other, it becomes feasible to comprehend how NPC diameter may differ considerably upon the action of mechanical forces.

In conclusion, the volumes reconstructed from these data reveal that many macromolecular complexes can be visually recognized without the need for computational averaging approaches and provide insight into structural variations at the level of individual complexes. Assisted by the synergistic application of recent technical developments, cryo-ET holds promise for revealing the molecular organization giving rise to cellular function in unperturbed environments.

REFERENCES AND NOTES

1. C. V. Robinson, A. Sali, W. Baumeister, *Nature* **450**, 973–982 (2007).
2. S. Pfeffer *et al.*, *Nat. Commun.* **6**, 8403 (2015).
3. F. K. Schur *et al.*, *Nature* **517**, 505–508 (2015).
4. M. Marko, C. Hsieh, R. Schalek, J. Frank, C. Mannella, *Nat. Methods* **4**, 215–217 (2007).
5. A. Rigort *et al.*, *J. Struct. Biol.* **172**, 169–179 (2010).
6. C. Hsieh, T. Schmelzer, G. Kishchenko, T. Wagenknecht, M. Marko, *J. Struct. Biol.* **185**, 32–41 (2014).
7. J. Mahamid *et al.*, *J. Struct. Biol.* **192**, 262–269 (2015).
8. R. Danev, S. Kanamaru, M. Marko, K. Nagayama, *J. Struct. Biol.* **171**, 174–181 (2010).
9. Y. Fukuda, U. Laugks, V. Lučić, W. Baumeister, R. Danev, *J. Struct. Biol.* **190**, 143–154 (2015).
10. P. Walther, Y. Chen, L. L. Pech, J. B. Pawley, *J. Microsc.* **168**, 169–180 (1992).
11. G. McMullan, A. R. Faruqi, D. Clare, R. Henderson, *Ultramicroscopy* **147**, 156–163 (2014).
12. S. Asano *et al.*, *Science* **347**, 439–442 (2015).
13. R. Danev, B. Buijsse, M. Khoshouei, J. M. Plitzko, W. Baumeister, *Proc. Natl. Acad. Sci. U.S.A.* **111**, 15635–15640 (2014).
14. Materials and methods and supplementary text are available as supplementary materials on *Science* Online.
15. S. Pfeffer *et al.*, *Nat. Commun.* **5**, 3072 (2014).
16. S. Pfeffer *et al.*, *Structure* **20**, 1508–1518 (2012).
17. K. H. Bui *et al.*, *Cell* **155**, 1233–1243 (2013).
18. T. Maimon, N. Elad, I. Dahan, O. Medalia, *Structure* **20**, 998–1006 (2012).
19. A. von Appen *et al.*, *Nature* **526**, 140–143 (2015).
20. U. Aebi, J. Cohn, L. Buhle, L. Gerace, *Nature* **323**, 560–564 (1986).
21. C. W. Akey, *J. Cell Biol.* **109**, 955–970 (1989).
22. E. Grossman *et al.*, *J. Struct. Biol.* **177**, 113–118 (2012).
23. K. Ben-Harush *et al.*, *J. Mol. Biol.* **386**, 1392–1402 (2009).
24. D. S. Fudge, K. H. Gardner, V. T. Forsyth, C. Riekel, J. M. Gosline, *Biophys. J.* **85**, 2015–2027 (2003).
25. N. Mücke *et al.*, *J. Mol. Biol.* **335**, 1241–1250 (2004).
26. J. Schäpe, S. Prausse, M. Radmacher, R. Stick, *Biophys. J.* **96**, 4319–4325 (2009).
27. K. Luger, A. W. Mäder, R. K. Richmond, D. F. Sargent, T. J. Richmond, *Nature* **389**, 251–260 (1997).
28. C. L. Woodcock, L. L. Frado, J. B. Rattner, *J. Cell Biol.* **99**, 42–52 (1984).
29. A. S. Frangakis *et al.*, *Proc. Natl. Acad. Sci. U.S.A.* **99**, 14153–14158 (2002).

ACKNOWLEDGMENTS

We are grateful to I. Poser for providing the HeLa cells; Y. Fukuda for advice on plunging; the local workshop for the design and production of tools; F. Beck and F. Bäuerlein for advice in data processing; P. Fratzl for advice on biomechanics; and D. Mastronarde for continuous developments in SerialEM and 3dmod. J.M. was supported by postdoctoral fellowships from the European Molecular Biology Organization and Human Frontier Science Program, and by the Weizmann Institute Women in Science Program. F.F. was supported by Deutsche Forschungsgemeinschaft grant FO 716/4. W.B. was supported by Center for Integrated Protein Science Munich. R.D. is a coinventor on a patent US 9129774 B2, "Method of using a phase plate in a transmission electron microscope," concerning the Volta phase plate. A.A.H. and W.B. are on the scientific advisory board of FEI Company. The supplementary materials contain additional data. EM densities have been deposited in the EMDataBank with the following accession numbers: EMD-8057, EMD-8056, EMD-8055, and EMD-8054.

SUPPLEMENTARY MATERIALS

www.sciencemag.org/content/351/6276/969/suppl/DC1
Materials and Methods
Supplementary Text
Figs. S1 to S10
Tables S1 to S3
References (*30*–*43*)
Movie S1

16 November 2015; accepted 22 January 2016
10.1126/science.aad8857

FOREST ECOLOGY

Leaf development and demography explain photosynthetic seasonality in Amazon evergreen forests

Jin Wu,[1]* Loren P. Albert,[1] Aline P. Lopes,[2] Natalia Restrepo-Coupe,[1,3] Matthew Hayek,[4] Kenia T. Wiedemann,[1,4] Kaiyu Guan,[5,6] Scott C. Stark,[7] Bradley Christoffersen,[1,8] Neill Prohaska,[1] Julia V. Tavares,[2] Suelen Marostica,[2] Hideki Kobayashi,[9] Mauricio L. Ferreira,[10,11] Kleber Silva Campos,[12] Rodrigo da Silva,[12] Paulo M. Brando,[13,14] Dennis G. Dye,[15] Travis E. Huxman,[16] Alfredo R. Huete,[3] Bruce W. Nelson,[2] Scott R. Saleska[1]*

In evergreen tropical forests, the extent, magnitude, and controls on photosynthetic seasonality are poorly resolved and inadequately represented in Earth system models. Combining camera observations with ecosystem carbon dioxide fluxes at forests across rainfall gradients in Amazônia, we show that aggregate canopy phenology, not seasonality of climate drivers, is the primary cause of photosynthetic seasonality in these forests. Specifically, synchronization of new leaf growth with dry season litterfall shifts canopy composition toward younger, more light-use efficient leaves, explaining large seasonal increases (~27%) in ecosystem photosynthesis. Coordinated leaf development and demography thus reconcile seemingly disparate observations at different scales and indicate that accounting for leaf-level phenology is critical for accurately simulating ecosystem-scale responses to climate change.

The seasonal rhythm of ecosystem metabolism—the aggregated photosynthesis, transpiration, or respiration of all organisms in a landscape—emerges from interactions among climate, ecology of individuals and communities, and biosphere-atmosphere exchange (*1*). In temperate zones, seasonality of terrestrial production drives annual oscillations in atmospheric carbon dioxide (*2*). In the tropics, plant transpiration seasonality mediates tropical convection and the timing of dry-to-wet season transitions—a potentially important climate feedback (*3*).

Seasonality in temperate zones is tightly linked to plant phenology (*4*) (the timing of periodic life-cycle events, including leaf development and senescence), which in turn is synchronized by cold-season dormancy (*4*). However, the extent, magnitude, and controls on seasonality of ecosystem metabolism in year-round warm tropical evergreen forest systems are less clear (*5*–*7*). For example, most current Earth system models represent little or no phenology in evergreen tropical biomes, so any seasonality in photosynthetic flux that emerges is due to seasonality in climatic drivers (*8*–*10*). However, remote-sensing observations (*5*–*7*, *11*–*13*) suggest that central Amazon forests seasonally increase their photosynthetic capacity ("green-up") during dry seasons, whereas southern Amazon and African tropical forests show declines (*13*). There is extensive debate over the mechanisms driving these patterns (including whether they might be remote-sensing artifacts) (*5*–*7*) and how they might be modeled (*8*–*10*, *14*).

To determine the extent of seasonality in tropical ecosystem photosynthesis (or gross ecosystem productivity, GEP), and to develop a more mechanistic understanding of how it emerges from climatic and biological processes, we address two key questions: (i) What is the relative importance of climatic drivers versus plant phenology in controlling GEP seasonality? (ii) What are the mechanisms by which these factors exert control? These questions conceptualize GEP as potentially driven by climate variability (e.g., temperature, light, or water) interacting with fixed photosynthetic infrastructure (e.g., leaf surface area, leaf photosynthetic capacity), or alternatively, by variability in that photosynthetic infrastructure, or some combination of the two.

To evaluate the first question, we compared GEP seasonality (derived from eddy covariance